Available online at www.sciencedirect.com
ScienceDirect
Journal of Molecular Catalysis A: Chemical 260 (2006) 157–162
JOURNAL OF MOLECULAR CATALYSIS A: CHEMICAL
www.elsevier.com/locate/molcata

Structure and redox properties of $Ce_xPr_{1-x}O_{2-\delta}$ mixed oxides and their catalytic activities for CO, CH_3OH and CH_4 combustion

Meng-Fei Luo *, Zong-Lan Yan, Ling-Yun Jin

Zhejiang Key laboratory for Reactive Chemistry on Solid Surfaces, Institute of Physical Chemistry, Zhejiang Normal University, Jinhua 321004, China

Received 18 July 2005; received in revised form 9 January 2006; accepted 4 July 2006
Available online 22 August 2006

Abstract

A series of $Ce_xPr_{1-x}O_{2-\delta}$ mixed oxides were synthesized by a sol–gel method and characterized by Raman, XRD and TPR techniques. The oxidation activity for CO, CH_3OH and CH_4 on these mixed oxides was investigated. When the value x was changed from 1.0 to 0.8, only a cubic phase CeO_2 was observed. The samples were greatly crystallized in the range of the value x from 0.99 to 0.80, which is due to the formation of solid solutions caused by the complete insertion of Pr into the CeO_2 crystal lattices. Raman bands at 465 and 1150 cm^{-1} in $Ce_xPr_{1-x}O_{2-\delta}$ samples are attributed to the Raman active F_{2g} mode of CeO_2. The broad band at around 570 cm^{-1} in the region of $0.3 \leq x \leq 0.99$ can be linked to oxygen vacancies. The new band at 195 cm^{-1} may be ascribed to the asymmetric vibration caused by the formation of oxygen vacancies. The TPR profile of Pr_6O_{11} shows two reduction peaks and the reduction process is followed: $PrO_{1.83} \xrightarrow{530\,^{\circ}C} PrO_{1.61} \xrightarrow{650\,^{\circ}C} PrO_{1.5}$. The reduction temperature of $Ce_xPr_{1-x}O_{2-\delta}$ mixed oxides is lower than those of Pr_6O_{11} or CeO_2. TPR results indicate that $Ce_xPr_{1-x}O_{2-\delta}$ mixed oxides have higher redox properties because of the formation of $Ce_xPr_{1-x}O_{2-\delta}$ solid solutions. The presence of the oxygen vacancies favors CO and CH_3OH oxidation, while the activity of CH_4 oxidation is mostly related to reduction temperatures and redox properties.

Keywords: $Ce_xPr_{1-x}O_{2-\delta}$; Solid solutions; Oxygen vacancies; Redox properties

1. Introduction

An oxygen-storage component is crucial for optimal performance of a three-way and emission-control catalyst. CeO_2 is extensively used in the three-way catalysts (TWCs). The primary function of CeO_2 in the TWCs is to provide oxygen-storage capacity (OSC), acting as an efficient "oxygen buffer" to undergo reduction/oxidation cycles by shifting between CeO_2 under oxidizing conditions (oxygen storage) and Ce_2O_3 under reducing conditions (oxygen release) [1]. Besides, CeO_2 can also promote the noble metal dispersion [2], increase thermal stability of Al_2O_3 support [3,4], and improve CO oxidation and water-gas shift reaction [5–7]. However, CeO_2 suffers significant deactivation of the redox couple, which occurs due to the sintering of CeO_2 particles and the reactions between CeO_2 and γ-Al_2O_3 support or active precious metals when it is performed at high temperatures under the driving conditions [8,9], resulting in the decline of OSC and the activity. In order to eliminate these drawbacks, a great number of CeO_2-based mixed oxide systems [10–18] such as Ce–Zr–O, Ce–Hf–O, Ce–La–O, Ce–Sn–O, Ce–Ti–O, Ce–Y–O and Ce–Pr–O have been conducted. Many studies have shown that the redox properties can be considerably enhanced if additional elements are introduced into the CeO_2 lattice and solid solutions are formed. Among the CeO_2-containing solid solutions, special attention has been focused on the Ce–Zr–O solid solution, which has been found to be very important to the three-way catalyst for cleaning the exhaust gases. From the reported results, the Ce–Zr–O solid solution shows the enhanced thermal stability, redox, and catalytic properties compared with ceria alone [19–21].

Praseodymium (Pr) has multiple stable oxidation states and it is one of the materials widely investigated because it undergoes more oxygen exchange at a lower temperature than ceria. Particularly, its oxygen-storage capacity is not diminished in case of high temperature sintering [22]. However, praseodymia seems not to be an effective replacement for ceria as an oxygen-storage

* Corresponding author. Fax: +86 579 2282595.
E-mail address: mengfeiluo@zjnu.cn (M.-F. Luo).

1381-1169/$ – see front matter © 2006 Elsevier B.V. All rights reserved.
doi:10.1016/j.molcata.2006.07.012

component. One major reason for that is a drastic difference in reactivity between ceria and praseodymia with alumina. Praseodymia can react with alumina at temperatures above 600 °C in air and can form inert aluminates, whereas ceria remains stable at 1100 °C [23]. Thus praseodymia can be used as an oxygen-storage material only if its reaction with alumina can be prevented. In recent years Ce–Pr–O mixed oxides have been widely studied, and they exhibit excellent catalytic properties [24,25]. When the system crystallizes into the face center cubic structure *fm3m*, because of the variable valency of Pr^{3+} or Pr^{4+}, a wide range of oxygen stoichiometry can exist [25]. The variable amount of oxygen ion vacancies produced can drastically change the properties of the formed solid solution. In order to gain more insight into the bulk and superficial structure of Ce–Pr–O mixed oxides, especially in respect of oxygen vacancies, the present work is devoted to preparing a series of $Ce_xPr_{1-x}O_{2-\delta}$ mixed oxides by a sol–gel method and to investigating their structures and reduction properties.

Volatile organic compounds (VOCs) and CO are recognized as major contributors to air pollution. Catalytic combustion is one of the most important processes for VOCs and CO destruction. So in this work, we reported the oxidation activity for CO and CH_4 combustion, and some interesting results were obtained. Oxygen vacancies created when Pr is substituted into a CeO_2 lattice play an important role in the CO oxidation. The $Ce_{0.5}Pr_{0.5}O_{2-\delta}$ sample shows a key high capability for oxygen storage and the highest catalytic activity for methane combustion.

2. Experimental

2.1. Catalysts preparation

A series of oxides with the general formula $Ce_xPr_{1-x}O_{2-\delta}$ ($x = 0$, 0.2, 0.3, 0.5, 0.7, 0.8,0.9, 0.95,0.97,0.99, 1.0) were prepared by a sol–gel method [18]. An appropriate amount of citrate acid solid powders was added into each pre mixed nitrate solution of cerium and praseodymium. The mixture was then vaporized under stirring until it became transparent gel. The gel was further dried at 100 °C and calcined at 500 °C for 4 h.

2.2. Characterization

X-ray diffraction (XRD) patterns were collected on a PHILIPS PW3040/60 powder diffractometer using Cu Kα radiation. The working voltage of the instrument was 40 kV and the current was 40 mA. The intensity data were collected at 25 °C in a 2θ range from 20° to 100° with a scan rate of 0.1 °/s. The high-temperature experiments were carried out using an X-ray reactor chamber XRK-900 Anton Paar, in which the scan rate was 0.2°/s and in the XRD patterns were recorded at the reduction atmosphere. The gas contained 5% H_2 and 95% N_2.

Raman spectra were obtained by a Renishaw RM1000 confocal microscope. The exciting wavelength was 632.8 nm from a He–Ne laser with a power of ca. 3 mW on the sample. The resolution is $\pm 1\ cm^{-1}$. In order to get the comparable data, the powder samples were pressed to form disks in a custom-made mold. The scanning range was 100–1300 cm^{-1}.

The reduction properties of $Ce_xPr_{1-x}O_{2-\delta}$ mixed oxides were determined by means of the TPR technique. The sample of $Ce_xPr_{1-x}O_{2-\delta}$ (50 mg) was placed in a quartz reactor. The reactor was heated from room temperature to 800 °C at a heating rate of 20 °C/min under flowing H_2–N_2 (5:95) with a total flow rate of 20 mL (NTP)/min (NTP: room temperature and 101.3 KPa).

The purpose of the reoxidation treatment was to reveal the oxidation properties of the reduced sample. After reduction at 800 °C, the reduction gas was switched off and the sample was cooled down to the desired oxidation temperatures (500, 100, and 50 °C, respectively), at which the oxidation took place under flowing air with a flow rate of 20 mL (NTP)/min for 0.5 h. Subsequently, the reoxidized samples were cooled to room temperature. Then, the TPR experiment was repeated.

2.3. Oxidation activity

Catalytic activity measurements were carried out in a fixed bed reactor (6 mm i.d.) filled with 150 mg catalyst powders. The total flow rate of the feed gas was 80 mL (NTP)/min. The catalysts were directly exposed to the reaction gas as the reaction temperature was reached without any pretreatment. For CO oxidation, the gas consisted of 2.4% CO, 1.2% O_2, and 96.4% N_2 with a total flow rate 80 mL (NTP)/min. For methane oxidation, the feed stream contained 3% CH_4, 8% O_2, and 89% N_2. The analysis of the CO_2 concentration in the reactor effluent was performed by means of a GC (13× molecular sieve and Propark Q) equipped with a thermal conductivity detector (TCD). For methanol oxidation, the concentration of CH_3OH was 4000 mg/m^3 in air. The analysis of CO_2 in the reactor effluent was performed on a TCD as the former. The analysis of the reactant and the organic compound in production were performed on a GC equipped with flame ionization detector (FID).

3. Results and discussion

3.1. XRD characterization of $Ce_xPr_{1-x}O_{2-\delta}$ mixed oxides

Fig. 1 shows the XRD patterns of $Ce_xPr_{1-x}O_{2-\delta}$ mixed oxides calcined at 500 °C. Crystalline phases were identified in comparison with two ICDD files (cubic CeO_2, PDF no. 81-0792; cubic Pr_6O_{11}, PDF no. 42-1121). From Fig. 1, it can be seen that the structure of all samples is fluorite-like, and the diffraction peaks are very close to each other, because the Ce^{4+} ionic radius (0.097 nm) is very similar to that of Pr^{4+} (0.096 nm). The peaks slightly shift to higher angles with the increasing x. In order to identify the phase composition, the pattern in the range from 45° to 50° of Fig. 1 was enlarged, as shown in Fig. 2. In the range of the value x from 0.3 to 0.7 the overlap diffraction peaks are observed in Fig. 2, indicating that both CeO_2 and Pr_6O_{11} phases are present in the $Ce_xPr_{1-x}O_{2-\delta}$ ($x = 0.3$–0.7) samples. This may be due to the fact that only a small amount of Pr can be introduced into the CeO_2 crystal lattices to form solid solutions, and the excess Pr remains in a single cubic phase. By increasing x from 0.80 to 0.99, the diffraction peaks become narrower and

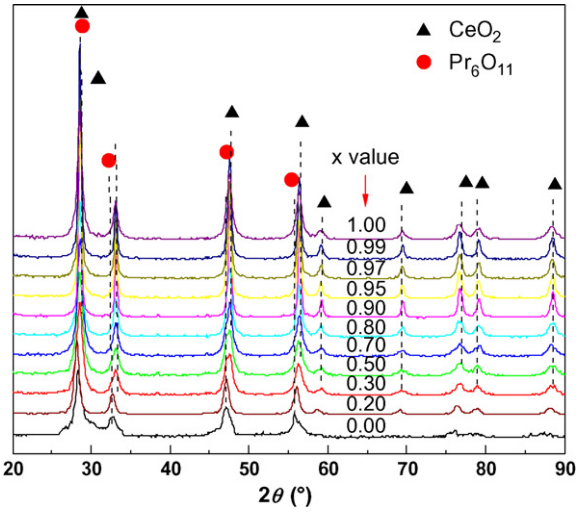

Fig. 1. XRD patterns of $Ce_xPr_{1-x}O_{2-\delta}$ mixed oxides calcined at 500 °C.

sharper. The results indicate that the samples are well crystallized, and the Pr completely inserts into the CeO_2 crystal lattices, resulting in the formation of the solid solutions.

3.2. Raman characterization of $Ce_xPr_{1-x}O_{2-\delta}$ mixed oxides

Fig. 3 shows the laser Raman spectra of the $Ce_xPr_{1-x}O_{2-\delta}$ mixed oxides calcined at 500 °C. It can be seen that for CeO_2 there are two obvious bands at 465 and 1170 cm^{-1}. The single sharp band at around 465 cm^{-1} is ascribed to the Raman active F_{2g} mode of CeO_2, the band of a fluorite structural material. This can be viewed as a symmetric breathing mode of the oxygen atoms surrounding each cation. Since only the oxygen atoms move, the mode frequency should be nearly independent of the cation mass [26]. The comparatively weak band at 1170 cm^{-1} can be due to primary A_{1g} asymmetry, combined with small additional contributions from E_g and F_{2g} symmetries [27]. No obvious Raman band is observed for Pr_6O_{11}. However, for $Ce_xPr_{1-x}O_{2-\delta}$ mixed oxides, four bands are observed at about 195, 465, 570 and 1150 cm^{-1}, respectively. Fig. 4 shows the laser Raman spectra of $Ce_{0.9}Pr_{0.1}O_{2-\delta}$ solid solution and physical mixture (Ce/Pr = 9/1) samples. The Raman bands at 195 and 570 cm^{-1} can be hardly seen for physical mixture sample. Thus, the Raman bands at 195 and 570 cm^{-1} for $Ce_{0.9}Pr_{0.1}O_{2-\delta}$ are attributed to the formation of the solid solution.

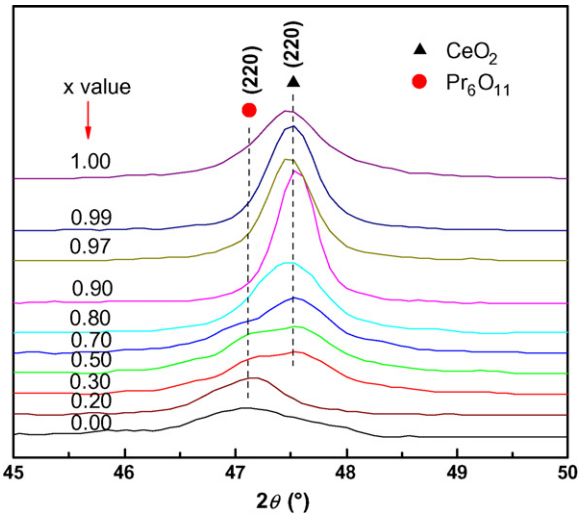

Fig. 2. Enlarged XRD patterns from the 2θ range from 45° to 50° in Fig. 1.

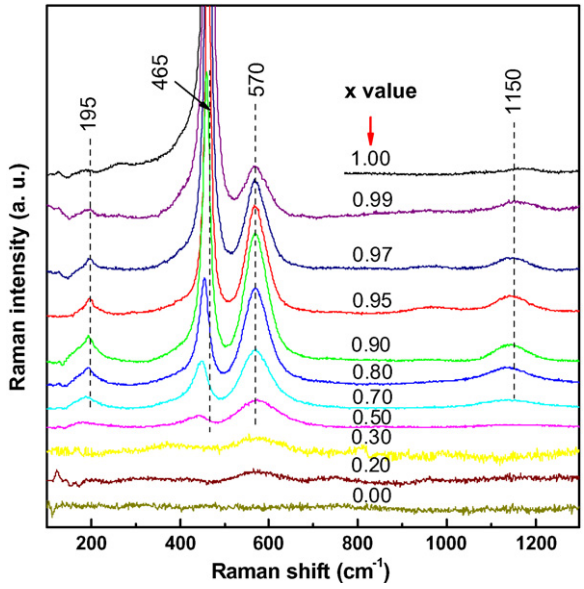

Fig. 3. Laser Raman spectra of $Ce_xPr_{1-x}O_{2-\delta}$ mixed oxides calcined at 500 °C.

In Fig. 3, it can be seen that there is a small systematic shift of the bands at 465 and 1170 cm^{-1} to lower frequencies with increasing Pr, because the atomic mass of Pr is larger than that of Ce and the insertion of Pr ions can decrease the vibration frequency of metal–anion band [26]. This also means that the incorporation of Pr into the ceria lattices results in the formation of the solid solutions. The intensity of the band at 465 cm^{-1} becomes weaker with increasing Pr content, while the broad

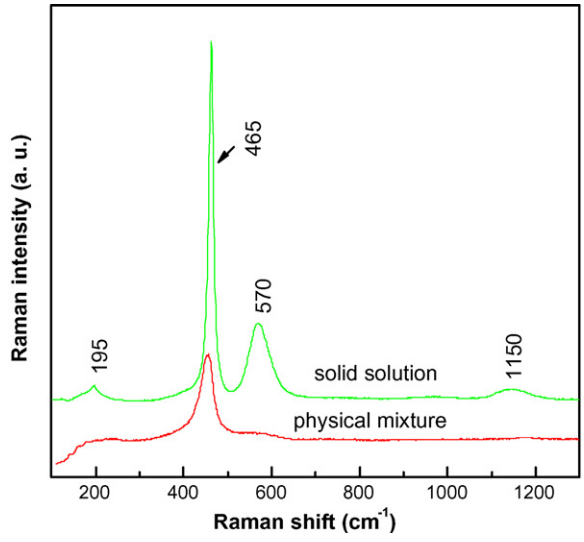

Fig. 4. Laser Raman spectra of $Ce_{0.9}Pr_{0.1}O_{2-\delta}$ solid solution and physical mixture (Ce/Pr = 9/1) sample.

peak around 570 cm^{-1} is distinct from the F_{2g} mode. McBride et al. [28] have reported that in Raman spectra the F_{2g} mode of $Ce_{1-x}RE_xO_{2-y}$ solid solutions becomes asymmetric with the presence of a long low-frequency tail as the value x increases, and there is also a weak band at about 570 cm^{-1} on the high frequency side of the band (Fig. 3). However, the presence of some defects can involve relaxation of the selection rules. In particular, this band has been linked to oxygen vacancies in the CeO_2 lattice [28]. The reason for the formation of the Raman band at 570 cm^{-1} is that when two Ce^{4+} ions are substituted by two Pr^{3+} ions, one oxygen vacancy is introduced into the fluorite lattice in order to maintain the electric neutrality, which will cause the broad peak on the high frequency side of the F_{2g} band. Thus the band at 570 cm^{-1} can be linked to lattice defects which results in the creation of oxygen vacancies. For $Ce_xPr_{1-x}O_{2-\delta}$ mixed oxides, the intensity of 570 cm^{-1} band reaches a maximum $x = 0.9$. Combined with the XRD patterns in Fig. 1, it is suggested that the perfect crystallite is formed and the oxygen vacancies are orderly arranged in the solid solutions in the case that the proportion of Ce and Pr can be well situated. Previously, oxygen vacancies in CeO_2 can be visualized to some extent only by scanning tunnelling microscopy (TEM) [29,30], and they are responsible for the enhanced OSC [31], because these oxygen vacancies can increase the diffusion rate of oxygen and absorb and give off oxygen easily [28]. The new band at 195 cm^{-1}, however, has not been reported in the previous literature. In Fig. 3, the changing trend of the intensity for the peak at 195 cm^{-1} is correlated to that of the peak at 570 cm^{-1}. Therefore, it can be pointed out that the new band at 195 cm^{-1} can be attributed to the other asymmetric vibration caused by the formation of oxygen vacancies. Further work on this topic will be carried out.

3.3. Redox properties

Fig. 5 shows the TPR profiles of the $Ce_xPr_{1-x}O_{2-\delta}$ mixed oxides calcined at 500 °C. There are two large reduction peaks at about 530 °C (α) and 650 °C (β) for Pr_6O_{11}. The *in situ* XRD

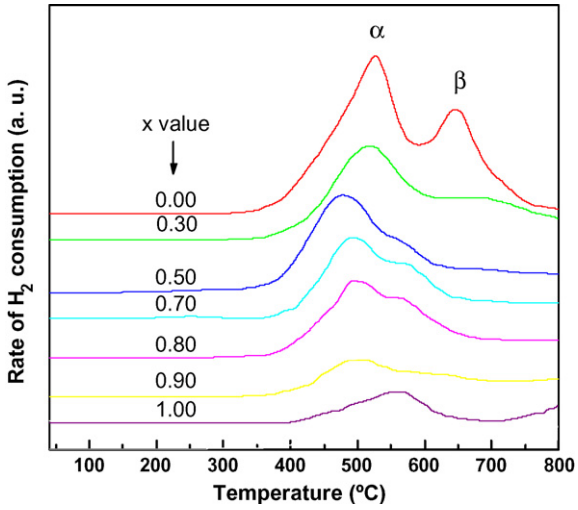

Fig. 5. TPRprofiles of $Ce_xPr_{1-x}O_2$ mixed oxides calcined at 500 °C.

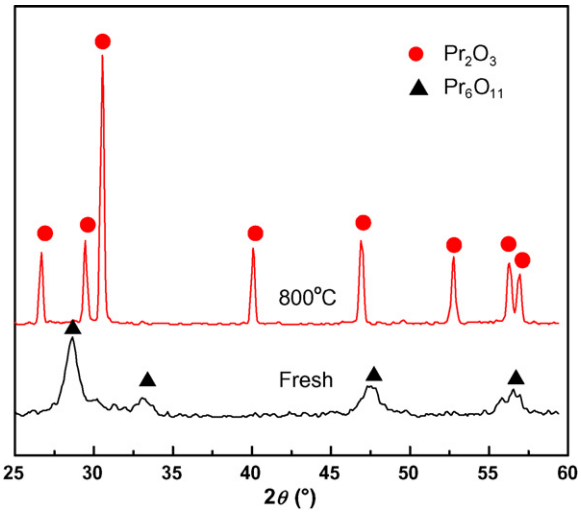

Fig. 6. *In situ* XRD patterns under the flowing mixture gas of H_2 (5%)–N_2 (95%) for the Pr_6O_{11} calcined at 500 °C.

patterns recorded under the reduction conditions are shown in Fig. 6, from which, it can be seen that Pr_6O_{11} is transformed to Pr_2C_3 completely after reduction at 800 °C. The ratio of α peak area to β peak area of Pr_6O_{11} in Fig. 6 is about 2:1. Therefore, it can be proposed that the reduction process of Pr_6O_{11} is followed as: $PrO_{1.83} \xrightarrow{530\,^{\circ}C} PrO_{1.61} \xrightarrow{650\,^{\circ}C} PrO_{1.5}$. For CeO_2, there are two small-reduction peaks at 570 °C and above 860 °C, respectively, which are associated with the stepwise reduction. The peak at 570 °C is generally attributed to reduction in the surface region, and the peak at temperatures above 860 °C is ascribed to the reduction of the bulk [20]. For $Ce_xPr_{1-x}O_{2-\delta}$ mixed oxides, when $x \leq 0.8$ there are two reduction peaks, which simultaneously shift to lower temperatures and additionally the β peak area obviously declines. Because of the weak reduction peak of CeO_2, it is believed that when $x \leq 0.8$ the reduction peaks of the samples are mainly attributed to the reduction of Pr^{4+} located on the surface and in the bulk. When $x = 0.5$, the temperature of the α reduction peak is the lowest (475 °C). When $x = 0.9$ both α and β reduction peaks become weak and the reduction peaks of the mixed oxide are similar to that of CeO_2. Generally, it is proposed that the generation of oxygen vacancies leads to the exchange of oxygen easily. Therefore, reactive oxygen species can be formed and are easily reduced by H_2 at a low temperature. In combination with the Raman spectra, it can be seen that the presence of the oxygen vacancies improves the reduction of solid solutions.

The redox behavior is a very important feature for most catalysts because there is a cycle process in oxidation reaction. Fig. 7 shows the TPR cycles of CeO_2, $Ce_{0.5}Pr_{0.5}O_{2-\delta}$, $Ce_{0.9}Pr_{0.1}O_{2-\delta}$, and Pr_6O_{11} at different reoxidation temperatures. For CeO_2 reoxidized at 500 °C, the reduction peak disappears at lower temperatures while at higher temperatures (>650 °C) it does not change significantly. There is a single reduction peak after reoxidation at 100 °C, while the reduction peak after reoxidation at 50 °C disappears for Pr_6O_{11}. However, for $Ce_{0.5}Pr_{0.5}O_{2-\delta}$ and $Ce_{0.9}Pr_{0.1}O_{2-\delta}$, the reduction peak areas increase after reoxidation even at 50 °C, while the peak shifts from 490 to 430 °C after

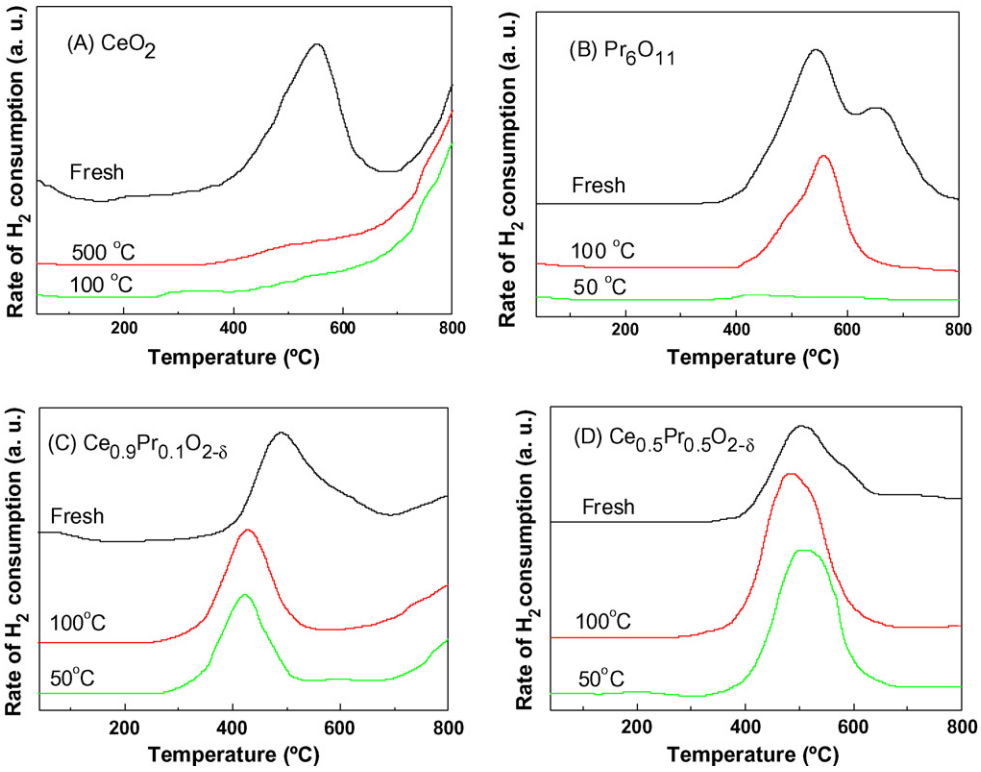

Fig. 7. TPR profiles of fresh samples and their reduced sample reoxidized at different temperatures. (A) CeO_2, (B) Pr_6O_{11}, (C) $Ce_{0.9}Pr_{0.1}O_{2-\delta}$, and (D) $Ce_{0.5}Pr_{0.5}O_{2-\delta}$.

reoxidation for $Ce_{0.9}Pr_{0.1}O_{2-\delta}$. However, the reduction peak temperature only slightly decreases for $Ce_{0.5}Pr_{0.5}O_{2-\delta}$ sample. This implies that the reduced $Ce_{0.5}Pr_{0.5}O_{2-\delta}$ and $Ce_{0.9}Pr_{0.1}O_{2-\delta}$ samples are easier to be reoxidized than CeO_2 and Pr_6O_{11}. In $Ce_{0.5}Pr_{0.5}O_{2-\delta}$ and $Ce_{0.9}Pr_{0.1}O_{2-\delta}$ samples, the enhanced redox properties are observed since the formation of solid solution with oxygen vacancies not only reduces the reduction temperature but also promotes the mobility of bulk oxygen. It is worthwhile noticing that the reduction peaks above 700 °C for CeO_2 and $Ce_{0.9}Pr_{0.1}O_{2-\delta}$ do not actually change obviously, indicating that the recovery of the high temperature peak is easy to be reoxidated.

3.4. Oxidation activity

Fig. 8 shows the relationship between T_{90} and Ce/(Ce + Pr) mole ratio for CO, CH_3OH and CH_4 oxidation, in which T_{90} represents the temperatures of 90% conversions. For CO oxidation, it has a maximum at $x = 0.9$ and a minimum at $x = 0.3$. From the XRD results (Fig. 2), the mixed phases of CeO_2 and Pr_6O_{11} are observed for $Ce_xPr_{1-x}O_{2-\delta}$ ($x = 0.3$–0.7). Thus it can be pointed out that the presence of the mixed phases inhibits CO oxidation activity. The oxidation activity is enhanced with further increasing the content of CeO_2 ($x = 0.3$–0.9). The highest oxidation activity occurs at $x = 0.9$ ($T_{90} = 350$ °C). While the oxidation activity decreases with further increasing the value x from 0.9 to 1.0. Combined with the Raman spectra in Fig. 3, it is found that stronger the intensity of the bands at 570 cm^{-1} is, the higher the oxidation activity for CO is. This implies the oxidation activity for CO is related to the oxygen vacancy. It is considered that CO can be easily absorbed at oxygen vacancies and then can react with neighboring oxygen atoms. Thus the high CO oxidation activity can be attributed to more facile generation of oxygen vacancies [32]. From Fig. 8, it can also be seen that the orderliness of the CH_3OH oxidation is similar to the CO oxidation. In particular the oxidation temperature for CH_3OH is lower than that for CO. The reason is that the polarity of CH_3OH (1.70 D) is bigger than that of CO (0.118 D), and CH_3OH is more easily absorbed on the oxygen vacancies than CO. As a result, for the oxidation of the polar small molecule,

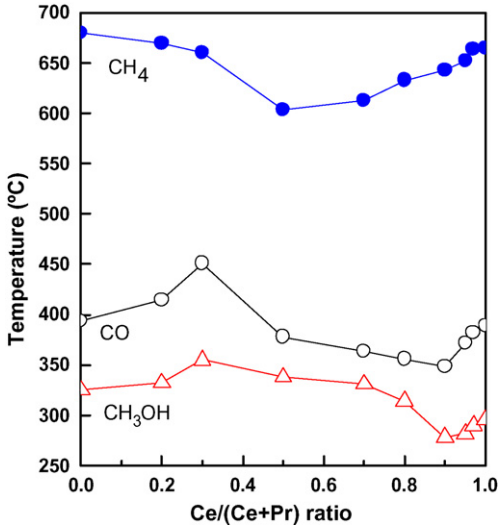

Fig. 8. T_{90} as a function of the molar ratio of Ce to (Ce + Pr) for CO, CH_3OH and CH_4 oxidation.

there is a certain corresponding relationship between the reaction activity and the number of the oxygen vacancies, which is larger, the activity for the oxidation of the polar small molecule is higher. For CH_4 oxidation, it can be seen that the oxidation temperature is higher than CO and CH_3OH oxidation. Moreover, a synergetic effect is observed, i.e. the oxidation activity of $Ce_xPr_{1-x}O_{2-\delta}$ mixed oxides is higher than that of both CeO_2 and Pr_6O_{11}. Additionally the $Ce_{0.5}Pr_{0.5}O_{2-\delta}$ sample shows the highest methane activity ($T_{90} = 600\,^{\circ}C$, $T_{50} = 530\,^{\circ}C$). The TPR profile (Fig. 7) indicates that $Ce_xPr_{1-x}O_{2-\delta}$ sample has the lowest temperature (475 °C) for α reduction peak. This shows that the oxidation activity for methane is related to the temperature and intensity of the reduction peak of the samples. There are two reasons for the low oxidation activity for methane. Firstly, methane is very stable and hard to be activated; secondly, there is a formation of H_2O during methane oxidation which might poison the oxygen vacancies. So for the combustion of methane the number of oxygen vacancies is not very important. Thus the high methane oxidation activity can be attributed to more mobility of bulk oxygen in catalysts. Though the formation of H_2O during CH_3OH oxidation, the polarity of CH_3OH (1.70 D) is similar to that of H_2O (1.85 D), so the effect of H_2O on the oxidation activity of CH_3OH is slighter than that on CH_4. Therefore, the changing rules of the oxidation activity of CH_3OH and CO are identical.

4. Conclusions

A series of $Ce_xPr_{1-x}O_{2-\delta}$ mixed oxides were characterized by various techniques such as XRD, TPR, and Raman. These mixed oxides were further used as catalysts for CO, CH_3OH and methane oxidation. XRD and Raman results indicate that the solid solution of $Ce_xPr_{1-x}O_{2-\delta}$ is formed via the incorporation of Pr into CeO_2 lattices. A single solid solution of $Ce_xPr_{1-x}O_{2-\delta}$ with a cubic phase is detected at $x = 0.8$–0.99. The Raman bands at about 465 and 1150 cm^{-1} are attributed to the Raman active F_{2g} mode of CeO_2. The broad peak at about 570 cm^{-1} in the region $0.3 \leq x \leq 0.99$ can be linked to lattice defects which results in oxygen vacancies. The insertion of Pr can be favorable for the formation of oxygen vacancies. The formation $Ce_xPr_{1-x}O_{2-\delta}$ solid solutions improve the reduction and reoxidation behavior. The activity of $Ce_xPr_{1-x}O_{2-\delta}$ for CO and CH_3OH oxidation implies that the presence of the oxygen vacancies favors CO and CH_3OH oxidation, while the activity of CH_4 oxidation is mostly related to reduction temperatures and redox properties.

Acknowledgment

The support by the Natural Science Foundation of China (Grant 20473075) is acknowledged.

References

[1] W.D. Wang, P.Y. Lin, Y.L. Fu, G.Y. Cao, Catal. Lett. 82 (2002) 19.
[2] F.L. Normand, K. Hilaire, K. Kili, G. Maire, J. Phys. Chem. 92 (1988) 2561.
[3] B. Harrison, A.F. Diwell, C. Hallett, Plat. Met. Rev. 32 (1988) 73.
[4] M. Ozawa, M. Kimura, J. Mater. Sci. Lett. 9 (1990) 291.
[5] J.G. Numan, H.J. Robota, M.J. Cohn, S.A. Bradley, J. Catal. 133 (1992) 309.
[6] C. Serre, F. Garin, G. Belot, G. Maire, J. Catal. 141 (1993) 1.
[7] M.F. Luo, Z.Y. Hou, X.X. Yuan, X.M. Zheng, Catal. Lett. 50 (1998) 205.
[8] S.J. Schmieg, D.N. Belton, Appl Catal. B: Environ. 6 (1995) 127.
[9] J.Z. Shyu, W.H. Weber, H.S. Gandhi, J. Phys. Chem. 92 (1988) 4964.
[10] J. Kaspar, P. Fornasiero, M. Graziani, Catal. Today 50 (1999) 285.
[11] P. Fornasiero, A. Speghini, R.D. Monte, M. Bettinelli, J. Kaspar, A. Bigotto, V. Sergo, M. Graziani, Chem. Mater. 16 (2004) 1938.
[12] F. Zamar, A. Trovarelli, C. Leitenburg, G. Dolcetti, J. Chem. Soc. Chem. Commun. (1995) 965.
[13] R.K. Usmen, G.W. Graham, W.L.H. Watkins, R.W. McCabe, Catal. Lett. 30 (1995) 53.
[14] R. Lin, Y.J. Zhong, T.H. Wu, M.F. Luo, W.P. Liu, J. Chin. Rare Earth Soc. 20 (2002) 203.
[15] M.F. Luo, J. Chen, L.S. Chen, J.Q. Lu, Z.C. Feng, C. Li, Chem. Mater. 73 (2001) 197.
[16] M.F. Luo, W.J. Shan, P.L. Ying, J.Q. Lu, C. Li, Stud. Surf. Sci. Catal. 138 (2001) 61.
[17] A. Gayen, K.R. Priolkar, P.R. Sarode, V. Jayaram, M.S. Hegde, G.N. Subbanna, S. Emura, Chem. Mater. 16 (2004) 2317.
[18] S. Bernal, G. Blanco, M.A. Cauqui, A. Martin, J.M. Pintado, A. Galtayries, R. Sporken, Surf. Interf. Anal. 30 (2000) 85.
[19] A. Trovarelli, Catal. Rev.-Sci. Eng. 38 (1996) 439.
[20] M.F. Luo, G.L. Lu, X.M. Zheng, Y.J. Zhong, T.H. Wu, J. Mater. Sci. Lett. 17 (1998) 1553.
[21] J.A. Rodriguez, J.C. Hanson, J.Y. Kim, G. Liu, A. Iglesias-Juez, M. Fernandez-Garcia, J. Phys. Chem. B 107 (2003) 3535.
[22] A.D. Logan, M.J. Shelef, Mater. Res. 9 (1994) 468.
[23] E.S. Putna, J.M. Vohs, R.J. Gorte, G.W. Graham, Catal. Lett. 54 (1998) 17.
[24] M.Y. Sinev, G.M. Graham, L.P. Haack, M. Shelef, J. Mater. Res. 11 (1960).
[25] A. Hartridge, Ghanashyam, M. Krishna, A.K. Bhattacharyta, Mater. Sci. Eng. B 57 (1999) 173.
[26] V.G. Keramidas, W.B. White, J. Chem. Phys. 59 (1973) 1561.
[27] W.H. Weber, K.C. Hass, J.R. McBride, Phys. Rev. B 48 (1993) 178.
[28] J.R. McBride, K.C. Hass, B.D. Poindexter, W.H. Weber, J. Appl. Phys. 6 (1994) 2435.
[29] H. Nörenberg, G.A.D. Briggs, Phys. Rev. Lett. 79 (1997) 4222.
[30] H. Nörenberg, G.A.D. Briggs, Surf. Sci. 402–404 (1998) 734.
[31] S. Rossignol, C. Descorme, C. Kappenstein, D. Duprez, J. Mater. Chem. 11 (2001) 2587.
[32] A.Q.M. Boon, F.V. Looij, J.W. Geus, J. Mol. Catal. 75 (1992) 277.